https://doi.org/10.48048/tis.2025.9264

Investigation of Acoustic Impedance and Morphology of Vacuum-Thermally Evaporated Polypyrrole Layer and Its Potential for Quartz Crystal Microbalance Sensor

Yudyanto[1,2], Masruroh[1,*], Dionysius J.D.H. Santjojo[1], Setyawan P. Sakti[1] and Arinto Yudi Ponco Wardoyo[1]

[1]Department of Physics, Faculty of Mathematics and Natural Sciences, Brawijaya University, Malang 65145, Indonesia
[2]Department of Physics, Faculty of Mathematics and Natural Sciences, Universitas Negeri Malang, Malang 65145, Indonesia

([*]Corresponding author's e-mail: ruroh@ub.ac.id)

Received: 3 November 2024, Revised: 30 November 2024, Accepted: 7 December 2024, Published: 20 January 2025

Abstract

This study investigated the influence of the morphology of a polypyrrole (PPy) functional layer on the acoustic impedance and PPy-QCM characteristics. In this study, the PPy thin layer was deposited on 1 side of QCM, following the dimension of the Au electrode. The layer production method yielded a simple design of a PPy-functionalized QCM. The impedance and PPy-QCM characteristics were determined by impedance analysis and microscopic observation. A vacuum thermal evaporation technique was used to deposit the PPy layer on the top of the QCM, allowing vertical platelet structure formation. Scanning Electron Microscope (SEM) images suggested that the deposition time increased the sizes of PPy but maintained their shapes. Analysis of impedance consisting of the conductance, bandwidth, and resonance frequency showed that changes in the layer morphology structure increased the resistance and the bandwidth (increasing energy dissipation and viscoelastic properties). As the deposition time increased from 10 to 50 s, the frequency shift experienced a significant increase from 6,000 to 32,000 Hz. This treatment also enlarged the bandwidth from 82 to 470 Hz. In addition, the impedance and load of QCM increased from 5.75 to 27.19 Ω and from 0.403 to 21.441 Ω, respectively. However, the deposition time in this range did not alter the stiffness properties of the layer. In other words, the thin PPy layer that was produced remained non-viscoelastic. The overall analyses in this study suggested that the PPy thin layer is promising for QCM sensing applications.

Keywords: Deposition time, Impedance, Layer morphology, Polypyrrole, QCM, Vacuum thermal evaporation

Introduction

In recent years, PPy has been one of the conductive polymers that have been widely studied due to its superior environmental stability and excellent conductivity compared to other conductive polymers [1-3]. It is extensively applied commercially as gas sensors [4-6], biosensors [7-9], and other applications [10,11]. Therefore, PPy is relevant as a primary sensor material.

In general, materials used as sensors are formed in a thin layer. A layer can be considered thin if it has a thickness ranging from nanometers to a few micrometers [12,13]. Various technologies for making thin films from materials include electrochemical deposition [14], dip-coating [15], spin-coating [16,17], Langmuir-Blodgett [18,19], Layer-by-layer (LBL) self-assembly [20], vapor deposition polymerization [21], DC Sputtering [22], and thermal evaporation [1,23,24]. Based on existing techniques, manufacturing a thin layer of pure PPy using thermal evaporation techniques has never been done. Therefore, it is argued that thermal evaporation is novel for the deposition of pure PPy. This technique has the advantage of being able to produce a thin layer, high-layer material purity, and low density

[25]. This low-density or many-pore layer suits gas, molecule, or particle sensors.

The PPy layer on a quartz crystal can be used as an adsorbent material in sensors based on changes in oscillation frequency to measure changes in mass. Recently, PPy-based QCMs have been applied for humidity sensing [26], gas detection [27], immunodetection [28], biomolecular characterization [29], and environmental monitoring [30]. The QCM sensor has high accuracy down to the nanogram level [31] under the stiffness characteristic of the functional layer. However, not all functional layers are rigid, as they must be compatible with the analyte. In this context, several researchers discovered a layer of pillar microstructure with viscoelastic properties [32-35].

This study uses vacuum thermal evaporation to produce a thin layer of PPy on top of QCM. The thin layer was prepared by varying the deposition time and controlling the amount of evaporated PPy mass. The novelty of this research is that it produces PPy layer morphology controlled easily through the vacuum-thermal evaporation method, where the deposition time can be varied. In addition, the correlation between the deposition time and changes in morphology, resonance frequency, and viscoelastic properties are analyzed.

Materials and methods

Materials and preparation

The PPy layer was prepared from PPy powder $H(C_4H_2NH)_nH$ obtained from Sigma-Aldrich (Product Number 577030, Singapore). PPy powder with the same mass of 50 mg was prepared for each deposition process. QCM with gold electrode was obtained from Shenzhen RenLux Crystal Co., Ltd. Before PPy coating, the surface of the QCM was cleaned by soaking it in acetone and sonicating it for 5 min.

Experimental method

The experimental procedures for PPy deposition on the QCM surface are presented in **Figure 1**.

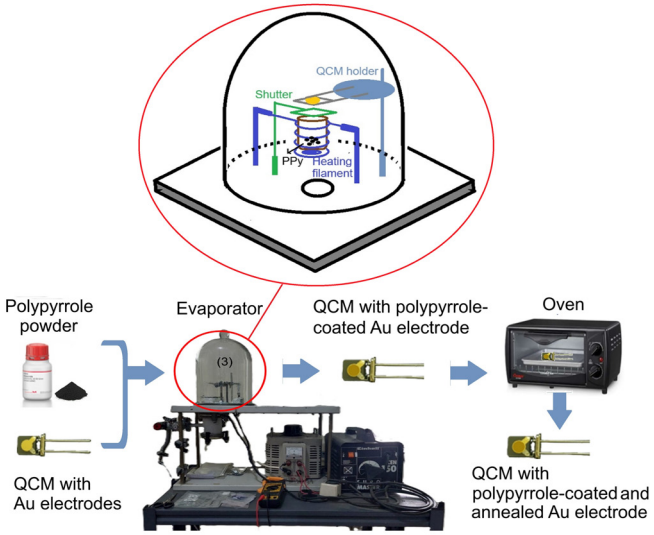

Figure 1 Procedures for coating PPy using the vacuum thermal evaporation technique.

The procedures presented in **Figure 1** are explained in the following. First, PPy powder with the same mass (50 mg) was prepared. Second, the PPy powder was inserted into the heating crucible tube in the evaporator, and the QCM was installed on the holder, positioned above the mouth of the heating crucible at a distance of 0.7 cm. The PPy deposition was carried out only on 1 side of the Au QCM electrode.

Each deposition process was carried out at air pressure in the evaporator of around 8 Pa with an electric voltage and current of 0.4 V and 27 A, respectively, as well as variations in the deposition time of 10, 20, 30, 40, and 50 s. Annealing was further carried out on all samples deposited with PPy at 900 °C in the oven for 1 h. The morphology of the PPy layer visible on the surface and side view was observed using a field emission scanning electron microscope (FESEM) type Quanta FEG 650 FEI Czech Republic s.r.o., Czech Republic. The thickness of the layer was determined from the height distribution of the platelet. The platelet

width and height distribution are described using ImageJ and OriginPro software. The ImageJ software was utilized to recognize the platelet shape from the image and measure the dimension within a particular scale. The measurement results were then visualized as the platelet size distribution graphs using OriginPro. Changes in QCM impedance values before and after PPy deposition were measured with a Bode 100 impedance analyzer, Omicron Electronics Asia Ltd., Hong Kong), with the equipment setup presented in **Figure 2**. The results of the impedance analysis set displayed real and imaginary impedance values, frequency, and phase differences.

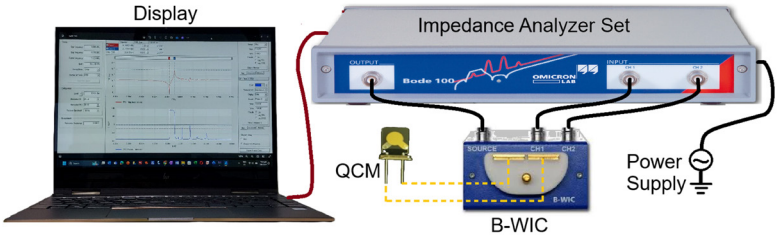

Figure 2 Set up for impedance measurement with Impedance analyzer Bode 100, Omicron Lab.

Results and discussion

Morphologies and their respective width distributions of the PPy layer on the surface of QCM with variations in deposition time of 10, 20, 30, 40, and 50 s are presented in **Figure 3**. And for the cross-section view of morphologies and their respective height distributions are presented in **Figure 4**. It can be seen that there is a change in the width and length of the structure, which becomes more prominent with the same thickness as the deposition time increases. The larger the width of the structure, the wider gaps between them appear, producing a larger open space [36]. The increasing size of the structures is due to the accumulation of PPy vapor as the deposition time increases. At 50 s of deposition, the PPy stacking pattern is clearly observed.

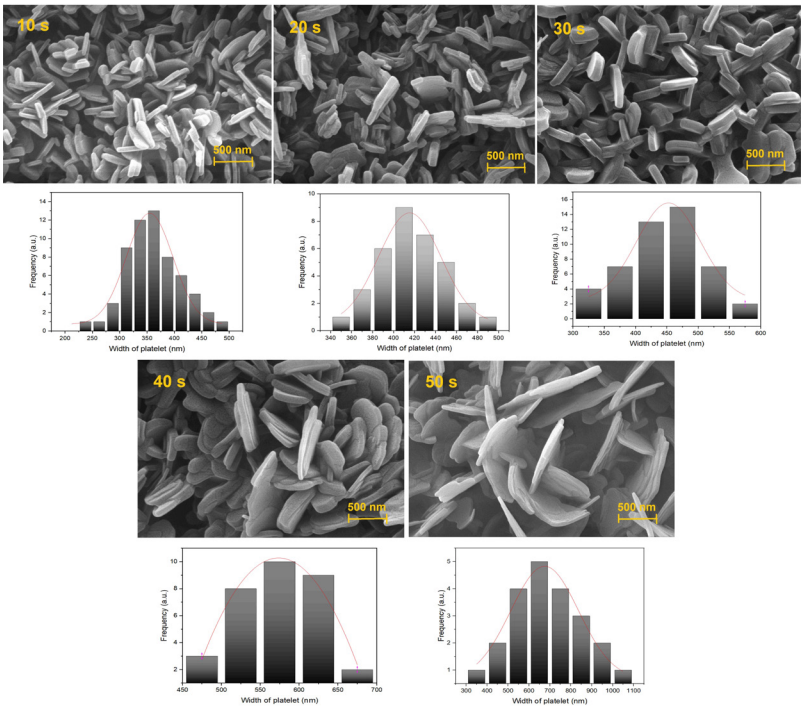

Figure 3 Morphologies and their respective width distributions of the PPy layer with variations in deposition time seen from the position above the surface.

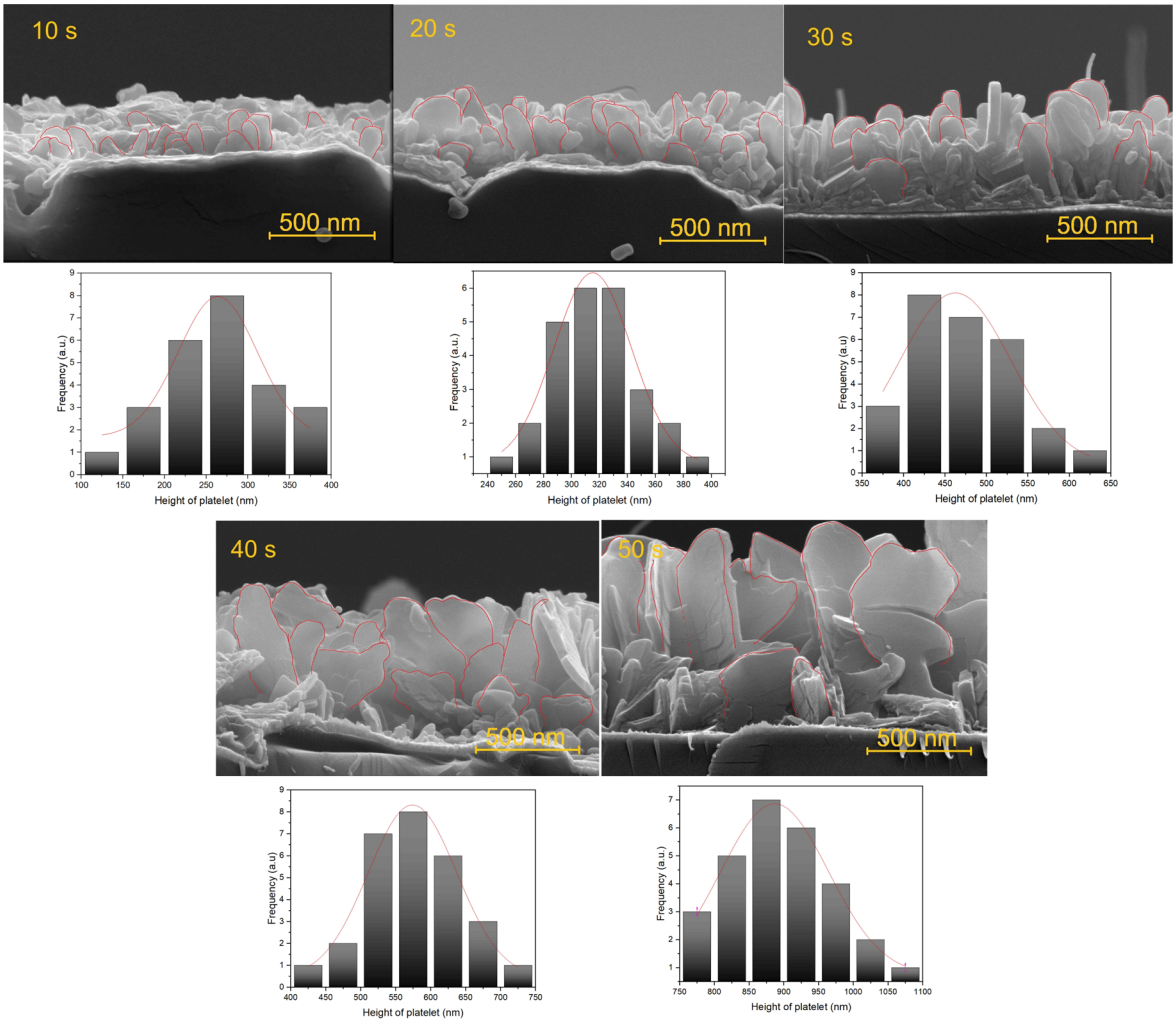

Figure 4 Morphologies and their respective height distributions of the PPy layer with variations in deposition time seen from the side position. The red line patterns depict the "leaf shape" platelet.

Figure 4 shows the changes in the leaf-shaped or platelet (red line patterns) that become wider and higher as the deposition time increases. The platelets are the result of agglomeration. The results of measurements of the average platelet width and height presented in **Table 1** support the observation of changes. **Figure 5** shows that the growth of the platelet's width and height has the same trend, but the average height of the platelet appears to be greater than the average width. With the increase of the deposition time, the thin layer will be thicker because the morphology of the platelet evolved from small to large.

Table 1 The average width and height of platelets.

Deposition time (s)	Width (nm)	Height (nm)
10	356.4 ± 2.4	256.4 ± 12.6
20	417.9 ± 4.0	321.5 ± 22.6
30	462.6 ± 11.4	465.3 ± 26.5
40	575.3 ± 11.1	576.2 ± 32.8
50	694.4 ± 24.6	893.5 ± 44.7

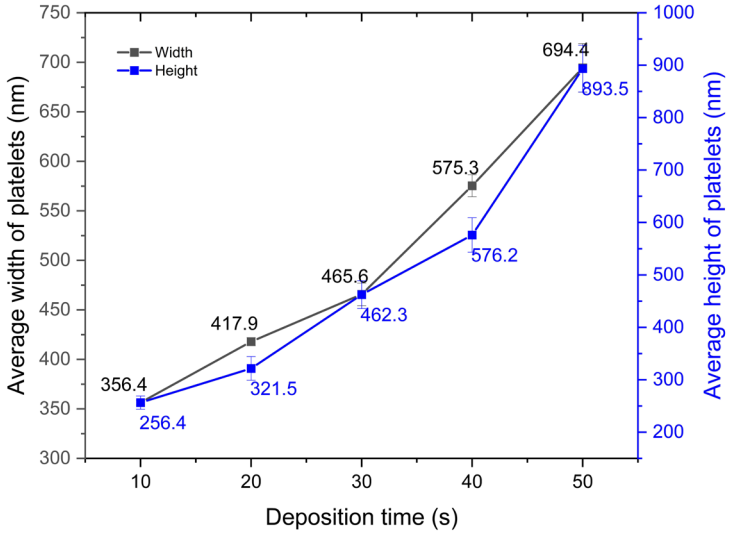

Figure 5 The effect of deposition time on platelets' average width and height.

Changes in the morphology of the QCM surface layer generally affect the damping of excessive oscillations and the viscoelastic character of the PPy-QCM. **Figure 6** presents the effect of deposition time on the magnitude and phase of the QCM impedance. Changes in the measured impedance illustrate the layer's mass distribution and mechanical response shift.

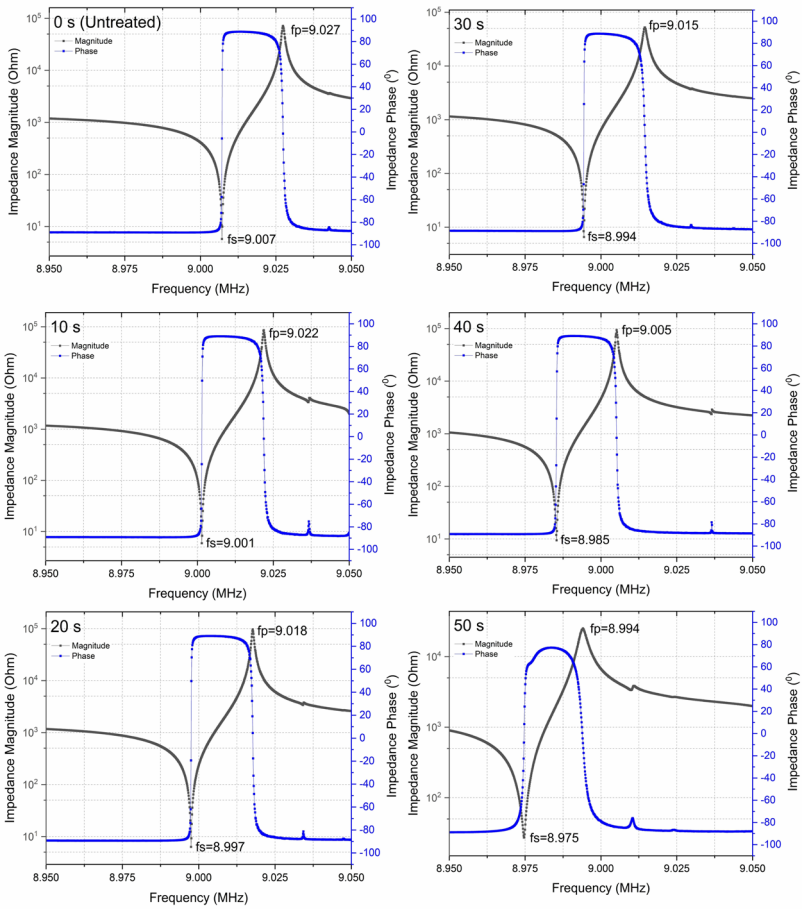

Figure 6 Effect of deposition time on impedance magnitude and phase.

As depicted in **Figure 6**, it is clear that the peak for the sample with a deposition time of 50 s has a more symmetrical parabolic shape in the phase impedance compared to the other 4 samples. It implied that the rigidity of the PPy layer deposited at 50 s was low. The other 4 samples showed identical peak shapes, with a sharp left edge but slightly curved on the right side. It suggested that deposition time larger than 50 s could contribute to higher impedance. On top of that, it is important to note that even though all samples have non-viscoelastic properties, the sample with a deposition time of 50 s has a higher degree of viscoelasticity as compared to the other 4 samples due to the peak shape of the phase impedance [37].

The results of the FESEM observations (**Figures 3** and **4**) show changes in the width and height of the PPy layer morphology due to the deposition time. During the deposition, initially, the PPy interacts with the gold electrode surface through physical bonds (such as van der Waals bonds) or covalent bonds. Free electrons of the metal interact with the electrons in the PPy structure on the surface of the gold electrode [38,39]. The covalent bond between Au and PPy, which can be easily removed, provides the advantage of QCM being reused. **Figure 7(a)** depicts the chemical reactions responsible for controlling the morphology of the PPy layer.

Furthermore, the structure variation starts from the growth of a small platelet (for 10 s deposition). The mechanism occurs due to the nature of PPy bonds, namely covalent bonds formed between carbon atoms in the pyrrole monomer, constructing long chains of PPy [40], as illustrated in **Figure 7(b)**. These bonds may give the growth shape of the PPy platelet form, which tends to be planar so that the platelet's thickness tends to remain unchanged [41]. The results show that the height of the platelet (perpendicular to the surface) is greater than the width of the platelet. This trend is caused by the stacking of platelets on the vertical side (height), which is more dominant than the addition of platelets in the horizontal direction (width); as shown in **Figure 8**, more PPy vapor sticks to the bottom side than to the side. Based on this occurrence, if the deposition time increases, the platelet pattern will also be more extensive, and the resulting voids between the platelets will be larger.

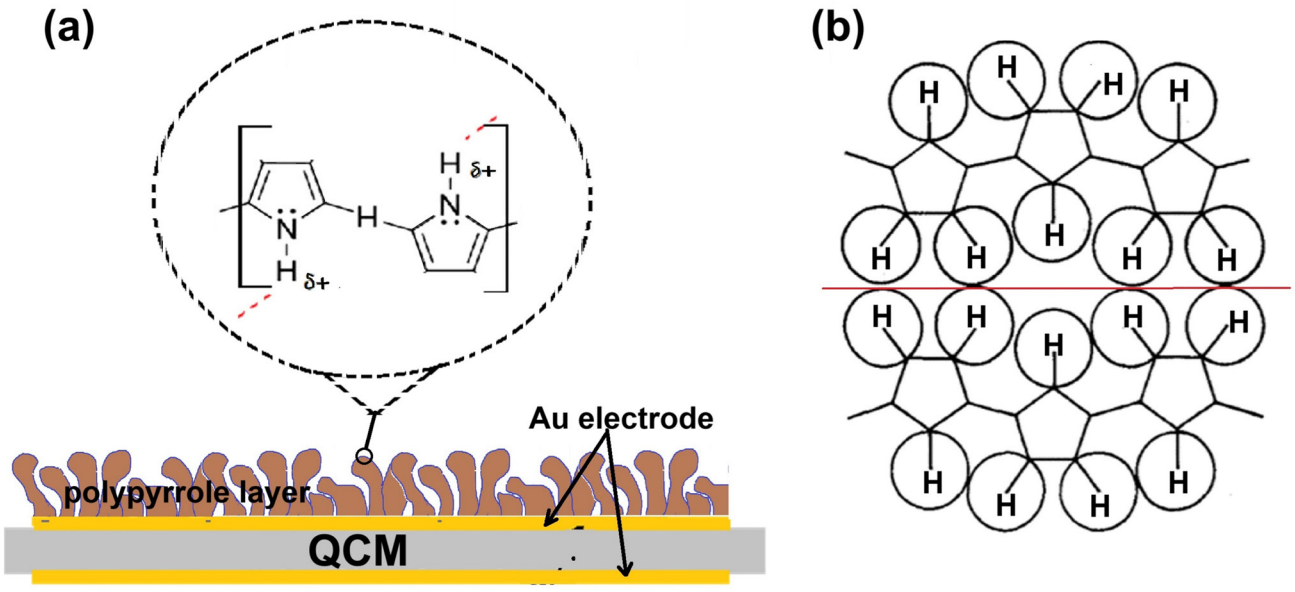

Figure 7 (a) Illustration of chemical reactions controlling PPy layer morphology, (b) Arrangement of neutral PPy chains with circles indicating diameter Van Der Waals of hydrogen, red lines indicate boundaries between chains one with another (this illustration is modified from [40]).

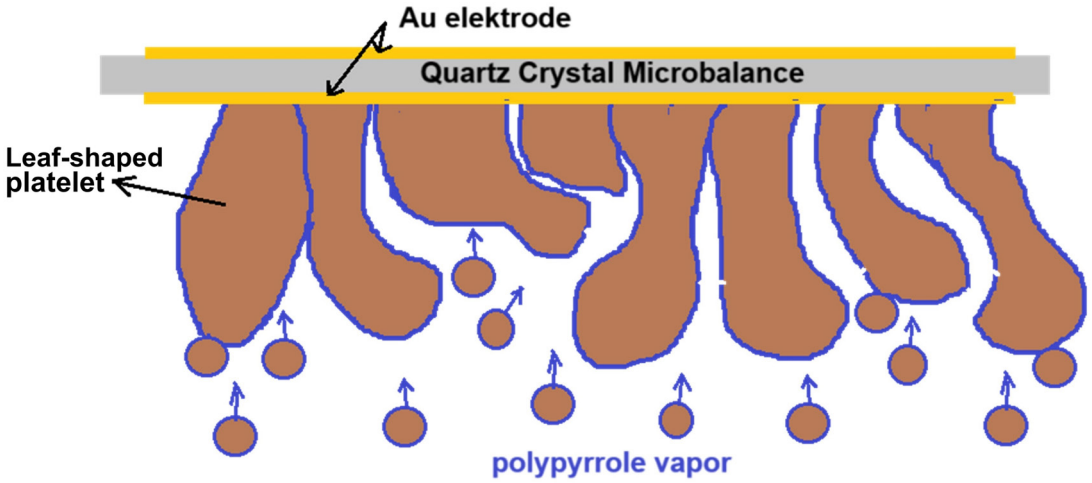

Figure 8 Mechanism of formation of PPy layer morphology through evaporation.

The effects of changes in the layer morphology and its characteristics were analyzed using impedance analysis. The results of impedance measurements are presented in **Figure 6**, while the results of conductance analysis, calculated from the impedance data, are presented in **Figure 9**. The results show that the conductance decreases as the deposition time increases. From **Figure 9**, it can be seen that there is a decrease in conductance (**Figure 9(b)**) along with increasing bandwidth and a shift in the resonance frequency towards a lower frequency (**Figure 9(a)**). This phenomenon is likely due to energy absorption, which is attributed to the effect of the PPy layer getting bigger in shape.

The frequency shift (Δf) presented in **Figure 10(a)** was obtained by calculating the relative difference between the PPy-coated QCM resonance frequency and the uncoated QCM resonance frequency (f_0 = 9.007 MHz). The resonant frequency depends on the impedance value (Z). The increasing impedance decreases the resonance frequency and conductance, causing a frequency shift towards lower frequencies.

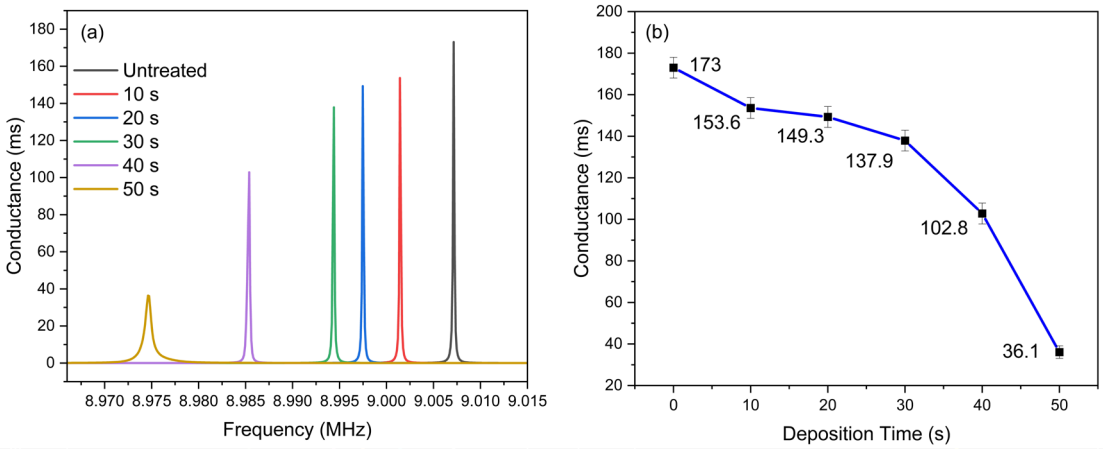

Figure 9 (a) Effect of deposition time on resonance frequency and conductance and (b) Effect of deposition time on conductance.

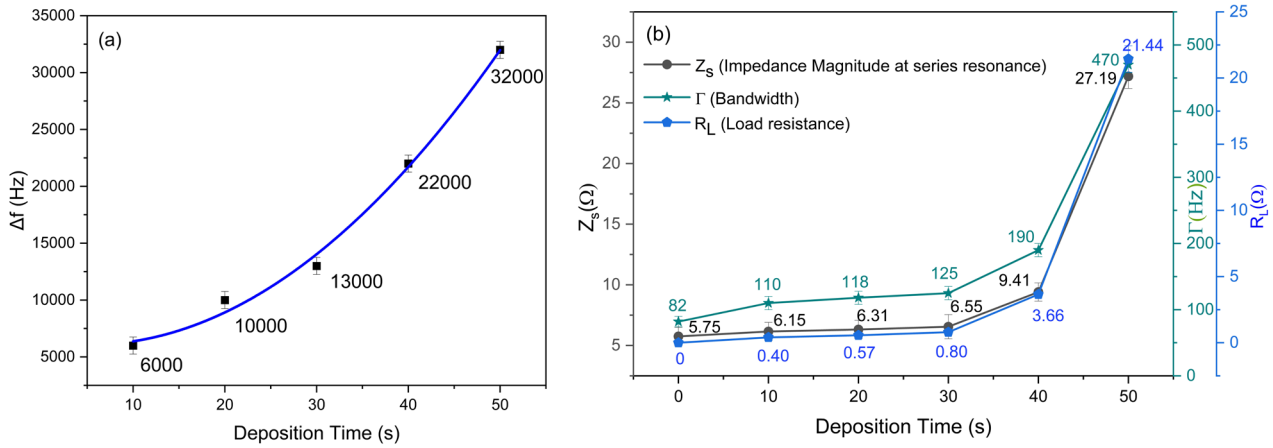

Figure 10 Effect of deposition time on (a); frequency shift; (b) bandwidth (Γ); impedance (Zs); and load resistance (RL).

Table 2 Shift of resonant frequency.

Deposition time (s)	f_s'(MHz)	$\|\Delta f\|$(MHz)
0 (Untreated)	9.007	0.000
10	9.001	0.006
20	8.997	0.010
30	8.994	0.030
40	8.985	0.022
50	8.975	0.032

Figure 10(b) shows that the bandwidth, impedance, and load resistance of the PPy layer increase as the deposition time increases due to larger PPy platelets (**Figures 3** and **4**). The larger platelets induce an increase in the QCM attenuation. Based on the data in **Table 2**, the change in resonance frequency (Δf) for all variations in deposition time carried out was less than 0.45035 MHz (equal to 5 % of the QCM resonance frequency without coating). Hence, it still fulfills the Sauerbrey equation, in which the thin layer on the QCM is still rigid.

Changes in frequency and viscoelastic properties of the layer in QCM are related to the amount of mass, stiffness of the layer material, and layer morphology. QCM provides real-time digital frequency output and is easy to operate [42]. Oscillations originate from the crystal's inherent resonant frequency, commonly called the resonant frequency. The size and thickness of the crystal determine the resonant frequency. Changes in the mass attached to the surface of the quartz crystal wafer cause changes in the crystal's resonant frequency. The relationship between changes in frequency and mass is expressed in the Sauerbrey equation [43].

$$\Delta f = -\frac{2nf_0^2}{A\sqrt{\rho_q \mu_q}}\Delta m \quad (1)$$

where n is odd wave number (n = 1, 3, 5, …), f_0 is the fundamental mode resonant frequency of the QCM without mass loading (Hz), Δf is the change in frequency (Hz), Δm is the change in mass (g), A is the active surface area of the QCM (cm^2), ρ_q is the density of quartz (2.648 g/cm^3), and μ_q is the shear modulus of quartz, and for crystals AT-cut (μ_q = 2.947×10^{11}g·cm^{-1}·s^{-2}).

Eq. (1) is suitable for oscillations in air. The thin layer of material stuck on top of the quartz is rigid, and the frequency changes $\Delta f/f < 0.05$ [44]. In reality, not all functional layers used have a rigid character in their operational frequency; some even have viscoelastic behavior, thus requiring a more complex equation model, as presented in the following [45].

$$\Delta f^* = \Delta f + i\Delta\Gamma \quad (2)$$

where ΔΓ is the change in half the bandwidth at half the maximum amplitude. The viscoelastic layer will

dissipate energy during oscillatory motion, reducing the quality factor value (Q).

Conclusions

A polypyrrole functional thin layer has been produced using a vacuum thermal evaporation deposition technique. The morphological structure of the resulting layer is in the form of platelets. The morphology evolved from small to large platelets due to changes in deposition time. The change of platelets has an impact on the thickness of the layer. The evolution in platelet size affects the impedance and PPy-QCM characteristics, including reducing conductance, increasing bandwidth (increasing energy dissipation and viscoelastic properties), and shifting the resonance frequency towards lower frequencies. However, this change has not shifted the stiffness of the layer (it is still non-viscoelastic). PPy-QCM offers superior sensing performance; it has the advantage of weak interaction between the PPy electrode and QCM, so the PPy layer is easy to remove, and QCM can be reused. However, PPy-QCM has the drawback of a sharp increase in impedance for a lengthy deposition time. Therefore, future research will focus on controlling the impedance increase caused by the layer morphology change. In addition, further research can be focused on improved PPy-QCM interaction for specific sensing applications, such as biosensing and environmental sensing.

Acknowledgments

The authors would like to thank Hibah Penelitian Unggulan (HPU) LPPM Universitas Brawijaya (UB), Indonesia 2022 and 2023 program for partially funding this research, Faculty of Mathematics and Natural Sciences Universitas Negeri Malang, Indonesia for supporting the publication, and Laboratorium Riset Terpadu (LRT) UB for SEM observation.

References

[1] A Attar, RD Alharthy, M Zwawi, M Algarni, F Albatati, M Bassyouni, MHA Aziz, MS Zoromba and AF Al-Hossainy. Fabrication and characterization of polypyrrole/multi-walled carbon nanotubes thin films using thermal evaporation. *Polymers* 2021; **13**, 22.

[2] A Husain and MU Shariq. Polypyrrole nanocomposites as promising gas/vapour sensing materials: Past, present and future prospects. *Sensors and Actuators A: Physical* 2023; **359**, 114504.

[3] PN Jadhav and KV Sukhatankar. Electrodeposition and characterization of polypyrrole films on stainless steel. *Materials Today Proceedings* 2023. https://doi.org/10.1016/j.matpr.2023.03.749.

[4] A Jain, AN Nabeel, S Bhagwat, R Kumar, S Sharma, D Kozak, A Hunjet, A Kumar and R Singh. Fabrication of polypyrrole gas sensor for detection of NH3 using an oxidizing agent and pyrrole combinations: Studies and characterizations. *Heliyon* 2023; **9(7)**, e17611.

[5] A Verma, R Gupta, AS Verma and T Kumar. A review of composite conducting polymer-based sensors for detection of industrial waste gases. *Sensors and Actuators Reports* 2023; **5**, 100143.

[6] X Liu, W Zheng, R Kumar, M Kumar and J Zhang. Conducting polymer-based nanostructures for gas sensors. *Coordination Chemistry Reviews* 2022; **462**, 214517.

[7] R Jain, N Jadon and A Pawaiya. Polypyrrole based next generation electrochemical sensors and biosensors: A review. *Trends in Analytical Chemistry* 2017; **97**, 363-373.

[8] D Zhang, X Lang, N Hui and J Wang. Dual-Mode electrochemical biosensors based on Chondroitin sulfate functionalized polypyrrole nanowires for ultrafast and ultratrace detection of acetamiprid pesticide. *Microchemical Journal* 2022; **179**, 107530.

[9] A Santos, APMDS Brandão, BM Hryniewicz, H Abreu, L Bach-Toledo, SSD Silva, AE Deller, VZ Rogerio, DSB Rodrigues, PM Hiraiwa, BG Guimarães, LF Marchesi, JCD Oliveira, DF Gradia, FLF Soares, NIT Zanchin, CCD Oliveira and M Vidotti. COVID-19 impedimetric biosensor based on polypyrrole nanotubes, nickel hydroxide and VHH antibody fragment: Specific, sensitive, and rapid viral detection in saliva samples. *Materials Today Chemistry* 2023; **30**, 101597.

[10] UD Chavan, P Prajith and B Kandasubramanian. Polypyrrole based cathode material for battery application. *Chemical Engineering Journal Advances* 2022; **12**, 100416.

[11] RB Choudhary, S Ansari and B Purty. Robust electrochemical performance of polypyrrole (PPy) and polyindole (PIn) based hybrid electrode materials for supercapacitor application: A review. *Journal of Energy Storage* 2020; **29**, 101302.

[12] PO Oviroh, R Akbarzadeh, D Pan, RAM Coetzee and TC Jen. New development of atomic layer deposition: Processes, methods and applications. *Science and Technology of Advanced Materials* 2019; **20(1)**, 465-496.

[13] A Rasool, S Kossar and R Amiruddin. *Different types of thin film deposition techniques and application*. *In*: YS Song, LR Thoutam, S Tayal, SB Rahi and TSA Samuel (Eds.). Handbook of emerging materials for semiconductor industry. Springer Nature Singapore, Singapore, 2024, p. 165-177.

[14] CJ Raj, R Manikandan, WG Lee, WJ Cho, KH Yu and BC Kim. Polypyrrole thin film on electrochemically modified graphite surface for mechanically stable and high-performance supercapacitor electrodes. *Electrochimica Acta* 2018; **283**, 1543-1550.

[15] S Jebali, M Vayer, K Belal, F Mahut and C Sinturel. Dip-coating deposition of nanocomposite thin films based on water-soluble polymer and silica nanoparticles. *Colloids and Surfaces A: Physicochemical and Engineering Aspects* 2024; **680**, 132688.

[16] P Temple-Boyer, L Mazenq, JB Doucet, V Conédéra, B Torbiéro and J Launay. Theoretical studies of the spin coating process for the deposition of polymer-based Maxwellian liquids. *Microelectronic Engineering* 2010; **87(2)**, 163-166.

[17] Z Zhou, S Zhou, X Cheng, W Liu, R Wu, J Wang, B Liu, J Zhu, BVD Bruggen and Y Zhang. Ultrathin polyamide membranes enabled by spin-coating assisted interfacial polymerization for high-flux nanofiltration. *Separation and Purification Technology* 2022; **288**, 120648.

[18] RDR Rodrigues, RLCGD Silva, L Caseli and LO Péres. Conjugated polymers as Langmuir and Langmuir-Blodgett films: Challenges and applications in nanostructured devices. *Advances in Colloid and Interface Science* 2020; **285**, 102277.

[19] D Roy, B Naskar and T Bala. Exploring Langmuir-Blodgett technique to investigate effect of various subphase conditions on monolayers formed by amphiphilic block co-polymers tetronic 701 and tetronic 90R4. *Colloids and Surfaces A: Physicochemical and Engineering Aspects* 2021; **625**, 126924.

[20] G Tidim, M Guzel, Y Soyer and I Erel-Goktepe. Layer-by-layer assembly of chitosan/alginate thin films containing *Salmonella enterica* bacteriophages for antibacterial applications. *Carbohydrate Polymers* 2024; **328**, 121710.

[21] CY Wu, PH Kuo and JG Duh. Reviving of silicon waste with N-doped carbon core-shell structure prepared by vapor deposition polymerization of polypyrrole applied in lithium-ion battery. *Surface and Coatings Technology* 2021; **421**, 127418.

[22] B Abdallah, R Hussin and W Zetoune. Effect of etched silicon substrate on structural, morphological, and optical properties of deposited ZnO films via DC sputtering. *Aerosol Science and Engineering* 2022; **6(1)**, 30-44.

[23] B Abdallah, M Kakhia and SA Shaker. Study of crystallographic, optical and sensing properties of Na_2WO_4 films deposited by thermal evaporation with several thickness. *Materials Science Poland* 2019; **37(4)**, 590-598.

[24] B Abdallah, M Kakhia and A Obaide. Morphological and structural studies of ZnO nanotube films using thermal evaporation technique. *Plasmonics* 2021; **16(5)**, 1549-1556.

[25] AS Kamenetskikh, NV Gavrilov, YS Surkov, PV Tretnikov and AV Chukin. Reactive deposition of Al_2O_3 coatings by thermal evaporation in a high-current discharge with a hollow anode. *Journal of Surface Investigation* 2020; **14**, 85-91.

[26] P Kumari, A Kumar, A Yadav, G Gupta, G Gupta, DD Shivagan and K Bapna. Chitosan-based highly sensitive viable humidity sensor for human health monitoring. *ACS Omega* 2023; **8(42)**, 39511-39522.

[27] S Öztürk, A Kösemen, Z Şen, S Tuna, SS Bayazit and N Kılınç. Highly sensitive and selective detection of dimethyl methyl phosphonate with copolymer-based QCM sensors. *Macromolecular Materials and Engineering* 2024; **309(5)**, 2300346.

[28] J Suthar, A Álvarez-Fernández, A Taylor, MJ Fornerod, GR Williams and S Guldin. Silica inverse opal nanostructured sensors for enhanced immunodetection of extracellular vesicles by quartz crystal microbalance with dissipation monitoring. *ACS Applied Nano Materials* 2022; **5(9)**, 12951-12961.

[29] J Wei, Y Shao, S Qiao, A Li, S Hou and WB Zhang. Biomacromolecular characterizations using state-of-the-art quartz crystal microbalance with dissipation. *Analytical Chemistry* 2023; **95(45)**, 16435-16446.

[30] JC Santos-Ceballos, F Salehnia, A Romero, X Vilanova and E Llobet. Low cost, flexible, room temperature gas sensor: Polypyrrole-modified laser-induced graphene for ammonia detection. *IEEE Sensors Journal* 2024; **24(7)**, 9366-9374.

[31] A Rehman and X Zeng. Monitoring the cellular binding events with Quartz Crystal Microbalance (QCM) biosensors. *Methods in Molecular Biology* 2017; **1572**, 313-326.

[32] NA Tehrani, IC Esfahani and H Sun. Simultaneous humidity and temperature measurement with micropillar enhanced QCM sensors. *Sensors and Actuators A: Physical* 2024; **366**, 115039.

[33] S Ji, H Esmaeilzadeh, J Su, S Pagsuyoin and H Sun. Novel analysis of a micropillar coupled acoustic wave sensor. *Sensors and Actuators Reports* 2021; **3**, 100034.

[34] J Su, H Esmaeilzadeh, P Wang, S Ji, M Inalpolat, M Charmchi and H Sun. Effect of wetting states on frequency response of a micropillar-based quartz crystal microbalance. *Sensors and Actuators A: Physical* 2019; **286**, 115-122.

[35] MAM Kashan, A Leong, T Saha, V Kalavally, V Swamy and N Ramakrishnan. QCM-micropillar-based coupled resonators in the detection of gas mass flow rates. *IEEE Transactions on Instrumentation and Measurement* 2019; **68(1)**, 303-305.

[36] H Wang, Y Wang, X Li, W Wang and X Yang. Influence of assembly gap size on the structure and properties of sus301L stainless steel laser welded lap joint. *Materials* 2021; **14(4)**, 996.

[37] R Etchenique and T Buhse. Viscoelasticity in the diffuse electric double layer. *Analyst* 2002; **127(10)**, 1347-1352.

[38] X Cui, VA Lee, Y Raphael, JA Wiler, JF Hetke, DJ Anderson and DC Martin. Surface modification of neural recording electrodes with conducting polymer/biomolecule blends. *Journal of Biomedical Materials Research* 2001; **56(2)**, 261-272.

[39] CG Wu, SC Chiang and CH Wu. Formation and electrochemical property of pyrrole-terminated SAMs and the effect of the SAMs on the physicochemical properties of polypyrrole films electrochemically deposited over them. *Langmuir* 2002; **18(20)**, 7473-7481.

[40] PPG Street, T Clarke, R Geiss, V Lee, A Nazzal and JS Uger. Characterization of polypyrrole (*in French*). *Journal de Physique Colloques* 1983; **44**, C3-599-C3-606.

[41] A Azioune, AB Slimane, LA Hamou, A Pleuvy, MM Chehimi, C Perruchot and SP Armes. Synthesis and characterization of active ester-functionalized polypyrrole-silica nanoparticles: Application to the covalent attachment of proteins. *Langmuir* 2004; **20(8)**, 3350-3356.

[42] L Wang, J Song and C Yu. The utilization and advancement of quartz crystal Microbalance (QCM): A mini review. *Microchemical Journal* 2024; **199**, 109967.

[43] G Sauerbrey. Verwendung von schwingquarzen zur wägung dünner schichten und zur mikrowägung (*in German*). *Zeitschrift für Physik* 1959; **155**, 206-222.

[44] AK Srivastava and P Sakthivel. Quartz-crystal microbalance study for characterizing atomic oxygen in plasma ash tools. *Journal of Vacuum Science & Technology A: Vacuum, Surfaces, and Films* 2001; **19(1)**, 97-100.

[45] Masruroh and DJDH Santjojo. The impedance analysis of a viscoelastic petalous structured stearic acid functional layer deposited on a QCM. *Sensors* 2022; **22(19)**, 7504.